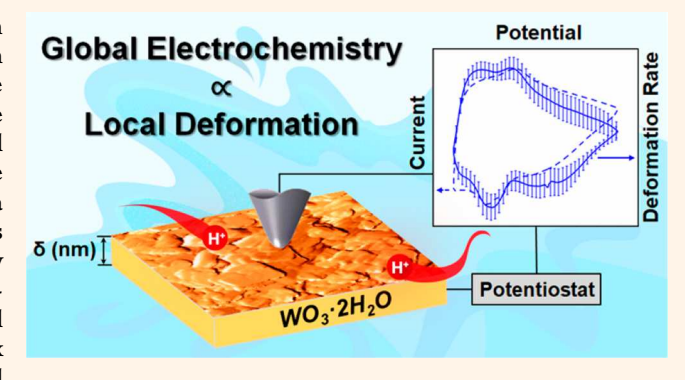


# Operando Atomic Force Microscopy Reveals Mechanics of Structural Water Driven Batteryto-Pseudocapacitor Transition

Ruocun Wang,<sup>†</sup> James B. Mitchell,<sup>†</sup> Qiang Gao,<sup>‡</sup> Wan-Yu Tsai,<sup>‡</sup> Shelby Boyd,<sup>†</sup> Matt Pharr,<sup>§</sup> Nina Balke,<sup>‡</sup> and Veronica Augustyn\*,<sup>†</sup>

Supporting Information

ABSTRACT: The presence of structural water in tungsten oxides leads to a transition in the energy storage mechanism from battery-type intercalation (limited by solid state diffusion) to pseudocapacitance (limited by surface kinetics). Here, we demonstrate that these electrochemical mechanisms are linked to the mechanical response of the materials during intercalation of protons and present a pathway to utilize the mechanical coupling for local studies of electrochemistry. *Operando* atomic force microscopy dilatometry is used to measure the deformation of redoxactive energy storage materials and to link the local nanoscale deformation to the electrochemical redox process. This technique reveals that the local mechanical



deformation of the hydrated tungsten oxide is smaller and more gradual than the anhydrous oxide and occurs without hysteresis during the intercalation and deintercalation processes. The ability of layered materials with confined structural water to minimize mechanical deformation likely contributes to their fast energy storage kinetics.

KEYWORDS: atomic force microscopy, interlayer engineering, nanoconfined water, energy storage, transition metal oxides

he intercalation of cations into the vacant sites of materials represents one of the most important electrochemical energy storage mechanisms and is widely used in commercialized rechargeable batteries. 1 Achieving high power capability while maintaining high energy density is desirable for numerous energy storage applications. Pseudocapacitance is an energy storage mechanism whereby transport processes in the solid state, such as diffusion, do not limit the faradaic reactions.<sup>3,4</sup> This property renders pseudocapacitance promising for achieving both high energy and power densities. The typical approach to increasing a material's pseudocapacitive response is by increasing its surface area, but from a fundamental and practical standpoint, it is desirable to determine alternative means of developing pseudocapacitive energy storage. In particular, as surface area increases, materials become more susceptible to parasitic side reactions and exhibit lower volumetric energy densities.<sup>5</sup> Recently, we discovered that the presence of structural water leads to a transition from battery to pseudocapacitive behavior in crystalline tungsten oxides.<sup>6</sup> The anhydrous, monoclinic WO<sub>3</sub> exhibits primarily diffusion-limited proton intercalation, whereas the hydrated, monoclinic  $WO_3 \cdot 2H_2O$  exhibits primarily surface-limited, or pseudocapacitive, proton intercalation. The rate capability and energy efficiency of the  $WO_3 \cdot 2H_2O$  is improved over that of  $WO_3$  despite similarity in particle morphology and surface area. The improvement in the kinetics of ion intercalation in hydrated tungsten oxides has been attributed to the presence of structural water. Structural water has also been shown to improve energy storage kinetics in transition metal oxides such as  $MnO_2$  and  $V_2O_5$ . In these materials, structural water has been hypothesized to decrease the activation energy required for interfacial charge transfer and/or ion diffusion. An underexplored question is whether the presence of structural water mitigates the mechanical deformation during ion intercalation, thus leading to fast energy storage kinetics.

The different kinetic responses for proton intercalation into WO<sub>3</sub>·2H<sub>2</sub>O and WO<sub>3</sub> bring into question whether the presence

 Received:
 March 26, 2018

 Accepted:
 May 16, 2018

 Published:
 May 16, 2018

<sup>&</sup>lt;sup>†</sup>Department of Materials Science & Engineering, North Carolina State University, Raleigh, North Carolina 27695, United States

<sup>&</sup>lt;sup>‡</sup>Center for Nanophase Materials Sciences, Oak Ridge National Laboratory, Oak Ridge, Tennessee 37830, United States

<sup>§</sup>Department of Mechanical Engineering, Texas A&M University, College Station, Texas 77842, United States

of structural water promotes different mechanical responses. For most materials, the electrochemical intercalation of cations leads to a change in the unit cell dimensions and/or phase of the structure to accommodate both the ion and increased electron density. 14,15 Since the current represents the change in capacity per time, a general relationship between the current and the rate of dimensional change may be written for a material undergoing deformation due to electrochemical ion intercalation:

$$i(E) = \frac{dQ(E)}{dt} \propto \frac{d\delta(E)}{dt}$$
 (1)

where i(E) is the current at a particular potential, Q(E) is the capacity at a particular potential, t is the time, and  $\delta(E)$  is the deformation of the material at a particular potential.<sup>16</sup> Because the accumulation of electrons and cations in the electrode results in a mechanical deformation of the host material, it follows that measuring the mechanical deformation could provide additional understanding of the enhanced rate capability of WO<sub>3</sub>·2H<sub>2</sub>O.

Here, we investigate the local mechanical response of WO<sub>3</sub> and WO<sub>3</sub>·2H<sub>2</sub>O to proton intercalation using atomic force microscopy (AFM) dilatometry, where the uniaxial electrode deformation is measured through the AFM tip displacement.<sup>17,18</sup> While several techniques are available to measure the total deformation of an electrode during energy storage using electrochemical dilatometry, 19-22 the methodology presented here provides a local and operando measurement with a temporal resolution as high as 100  $\mu$ s (limited by AFM instrument electronics) and a lateral resolution on the order of tens of nanometers (limited by the AFM tip dimension). This approach has been used to study purely capacitive and pseudocapacitive energy storage systems, 17,18 but has never been applied to battery-type materials. We show that the anhydrous, battery-type tungsten oxide exhibits a hysteresis in the electrode deformation as a function of potential, whereas the hydrated, pseudocapacitive tungsten oxide shows little to no hysteresis. In addition, the overall deformation of the hydrated tungsten oxide is smaller even when a greater number of electrons is stored per formula unit than in the anhydrous oxide. We also demonstrate that the deformation rate is directly proportional to the energy storage current in intercalation-type oxides and that it exhibits the same kinetic dependence as the current for diffusion and capacitive processes. This is a very important finding, which connects the local mechanical signature (measured with nanoscale lateral and axial resolution) to the electrochemical redox process. It also provides an opportunity to study local electrochemical redox processes that are not attainable with current-based techniques. The deformation is mapped as a function of position in the electrode to demonstrate the ability of operando AFM dilatometry to probe local changes in the electrode deformation as a function of ion storage. Together, these methods allow for local studies of mechanically coupled electrochemical processes since the deformation is measured with a lateral resolution of tens of nanometers with the AFM probe. Our results show that proton intercalation in hydrated tungsten oxides produces a highly reversible and homogeneous mechanical response. In addition, these results suggest that the role of structural water in hydrated tungsten oxide may be to enable facile mechanical deformation by decreasing the number of primary bonds that deform during proton intercalation.

#### RESULTS AND DISCUSSION

To determine the mechanical response of  $WO_3 \cdot nH_2O$  (n = 0 or 2) during electrochemical proton intercalation, thin film electrodes were fabricated by drop-casting WO<sub>3</sub>·nH<sub>2</sub>O particles onto a glassy carbon electrode. The morphology and thickness of the electrodes were measured with scanning electron microscopy (SEM) (Figure S1). The particle-based films of both oxides were  $\sim$ 370–480 nm thick, with larger and smaller aggregates throughout. The surface morphology of the dry electrodes was measured using AFM and is shown in Figure 1a and c. From our prior results, the platelet-like particles of WO<sub>3</sub>·2H<sub>2</sub>O are oriented in the [010] direction.

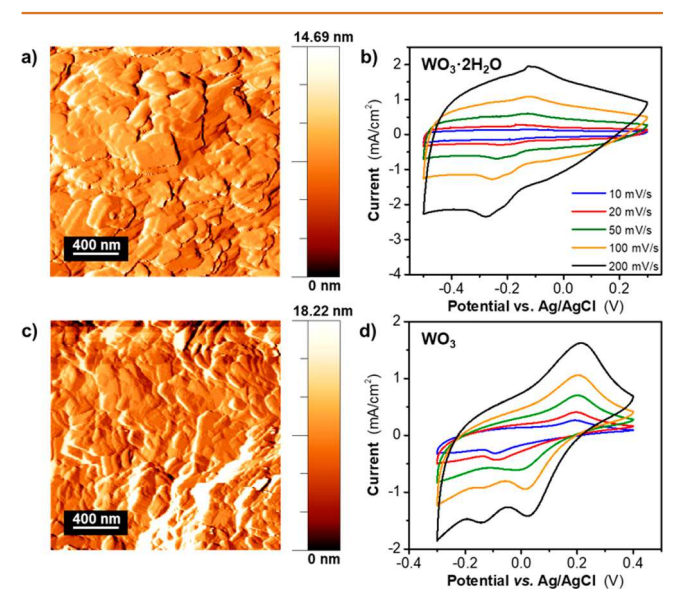


Figure 1. Surface morphology and electrochemical characterization of WO3 and WO3·2H2O electrodes obtained from the in situ electrochemical AFM cell. (a, c) Deflection images of the thin film electrode surface of WO<sub>3</sub>·2H<sub>2</sub>O (a) and WO<sub>3</sub> (c). (b, d) Cyclic voltammograms of WO<sub>3</sub>·2H<sub>2</sub>O (b) and WO<sub>3</sub> (d) electrodes in 0.5 M  $H_2SO_4$  at sweep rates ranging of 10–200 mV s<sup>-1</sup>.

Proton intercalation into WO<sub>3</sub>·nH<sub>2</sub>O may be written as

$$WO_3 \cdot nH_2O + xH^+ + xe^- \leftrightarrow H_xWO_3 \cdot nH_2O$$
 (2)

where the maximum amount of proton intercalation (x) is typically <1,<sup>23</sup> for a capacity of 417 C g<sup>-1</sup> for WO<sub>3</sub> and 360 C g-1 for WO<sub>3</sub>·2H<sub>2</sub>O. In aqueous acidic electrolytes, the maximum intercalation capacity is not reached due to the onset of the hydrogen evolution reaction. Figure 1b and d show the cyclic voltammograms of WO<sub>3</sub>·nH<sub>2</sub>O in 0.5 M H<sub>2</sub>SO<sub>4</sub> electrolyte from 10 to 200 mV s<sup>-1</sup> (t = 3.5-70 s) in the *in situ* electrochemical AFM cell (Figure S2). The specific capacitance values at these sweep rates are presented in Figure S3. As in prior reports, the in situ AFM cell results demonstrate that proton storage in WO<sub>3</sub>·2H<sub>2</sub>O is a more reversible process than in WO<sub>3</sub> as observed from the increased symmetry of the cyclic voltammograms over all sweep rates. Due to the thin film architecture, the in situ cell results are limited to sweep rates of >10 mV s<sup>-1</sup> as there is a significant current contribution from the hydrogen evolution reaction at slower rates.

The deformation  $(\delta, \text{ in nm})$  of the thin film electrodes was measured as a function of applied potential and at different cyclic voltammetry (CV) sweep rates using the in situ AFM cell. Figure 2a and b show the local deformation of each electrode as

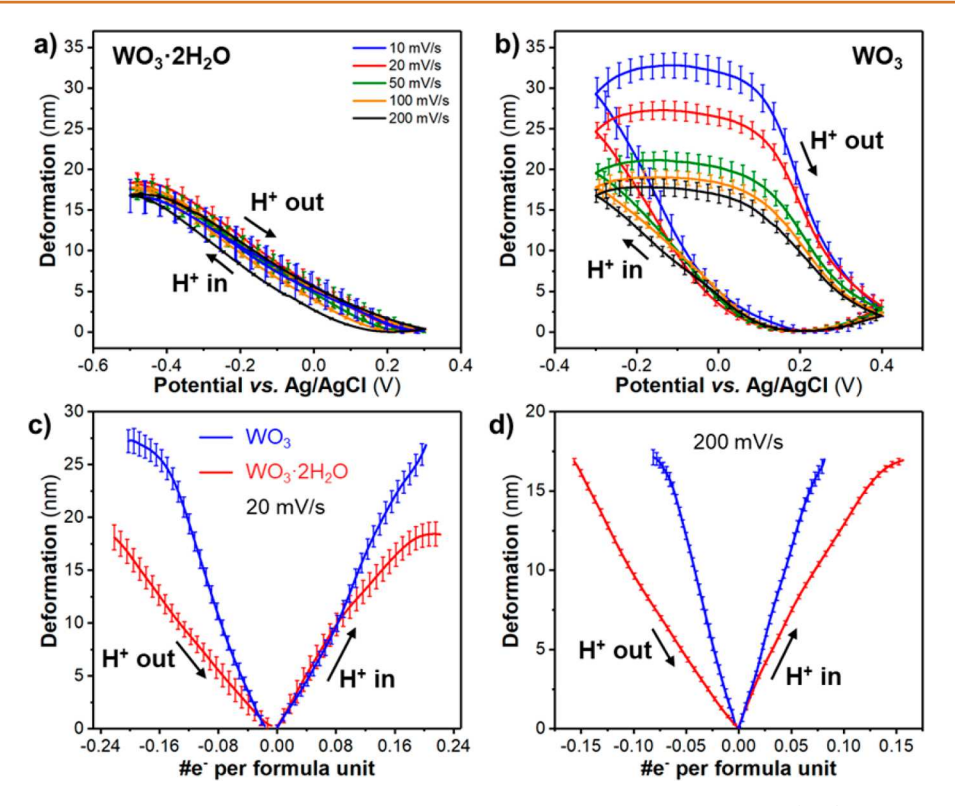


Figure 2. Local deformation of WO<sub>3</sub> and WO<sub>3</sub>·2H<sub>2</sub>O electrodes as a function of potential and capacity. (a, b) Deformation *versus* potential at different cyclic voltammetry sweep rates of WO<sub>3</sub>·2H<sub>2</sub>O (a) and WO<sub>3</sub> (b). Error bars indicate the standard deviations of the deformation at specific potentials for 18 cycles. (c, d) Deformation *versus* number of electrons per formula unit of WO<sub>3</sub> and WO<sub>3</sub>·2H<sub>2</sub>O at sweep rates of 20 mV s<sup>-1</sup> (c) and 200 mV s<sup>-1</sup> (d). Error bars indicate the standard deviations of the deformation at specific numbers of electrons per formula unit. A negative number of electrons represents the anodic cycle, and a positive number of electrons represents the cathodic cycle.

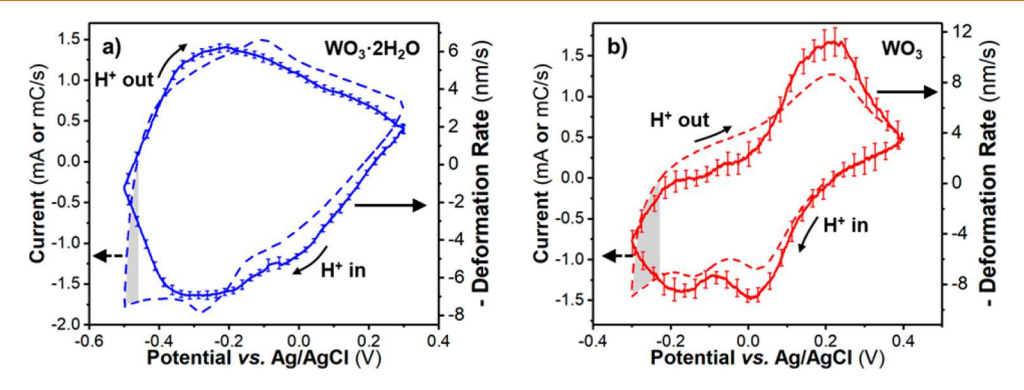


Figure 3. Correlation between the local deformation rate and the global electrode current. (a, b) Average deformation rate (solid line) and current (dashed line) *versus* potential at a sweep rate of 200 mV s<sup>-1</sup> for WO<sub>3</sub>·2H<sub>2</sub>O (a) and WO<sub>3</sub> (b). Error bars indicate the standard deviations of the deformation rate at specific potentials. The shaded area indicates the regions of potential where the hydrogen evolution reaction contributes to the total current.

a function of potential from 10 to 200 mV s<sup>-1</sup>. At all sweep rates, the WO<sub>3</sub>·2H<sub>2</sub>O exhibits a highly reversible and almost linear deformation for both the cathodic and anodic sweeps, indicating that the intercalation and deintercalation processes occur at approximately the same potentials and are thus highly reversible. Such a response would be expected from the broad, symmetric shape of the CV for WO<sub>3</sub>·2H<sub>2</sub>O. On the other hand, at all sweep rates, WO<sub>3</sub> exhibits nonlinear deformation and hysteresis between the anodic and cathodic sweeps. This hysteresis indicates that intercalation and deintercalation deformation do not occur at the same potentials and are thus less reversible. The electrode deformation depends on the capacity, or number of electrons stored per formula unit. Figure

2c and d show that at both 20 and 200 mV s<sup>-1</sup> the overall deformation is smaller for  $WO_3 \cdot 2H_2O$  even when the number of stored electrons is greater than in  $WO_3$ . Overall, these observations indicate differences in the mechanical response to intercalation between  $WO_3 \cdot 2H_2O$  and  $WO_3$ , similar to their differences in the current response to intercalation.

Since current (i) is the rate of change of the capacity (Q), the current can be expressed as dQ  $dt^{-1}$ , and a cyclic voltammogram is plotted as the "capacity rate" as a function of potential. We were interested in determining whether the deformation rate  $(d\delta \ dt^{-1})$  also depends upon potential. Interestingly, as shown in Figure 3, we found that the deformation rate exhibits almost the same dependence on the potential as the capacity

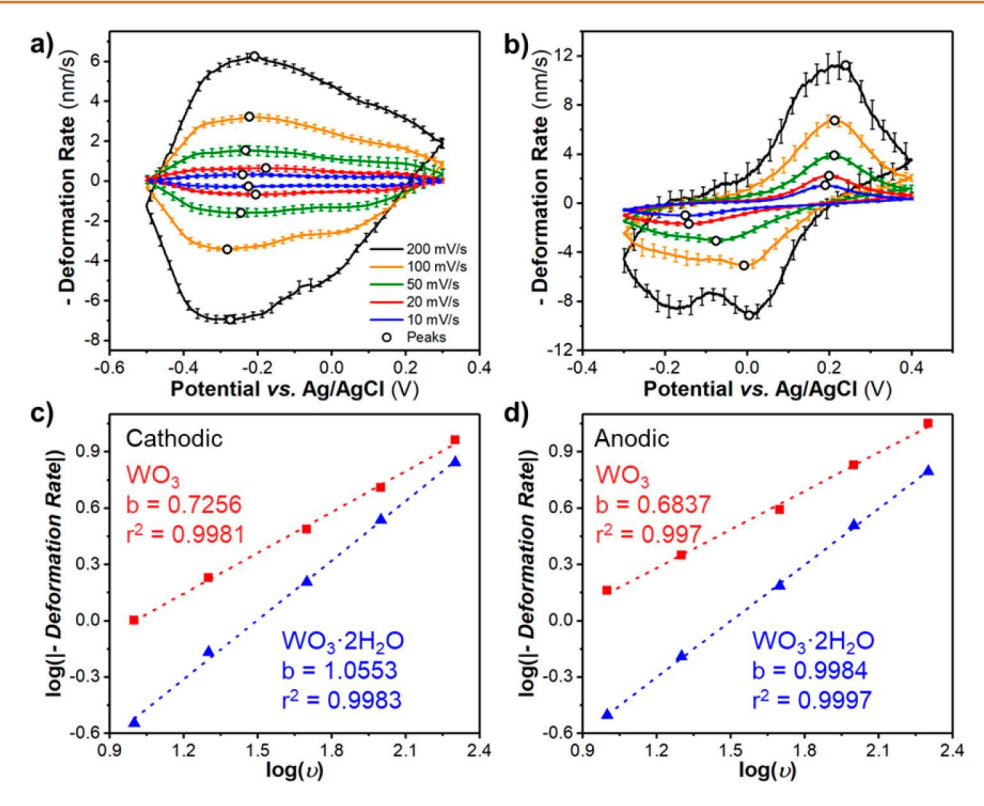


Figure 4. Kinetic analysis of the local deformation rate of WO<sub>3</sub> and WO<sub>3</sub>·2H<sub>2</sub>O. (a, b) Deformation rate *versus* potential at sweep rates from 10 to 200 mV s<sup>-1</sup> for WO<sub>3</sub>·2H<sub>2</sub>O (a) and WO<sub>3</sub> (b). The circles indicate the deformation rate peak values used for *b*-value determination. Error bars indicate the standard deviations of the deformation rate at specific potentials. (c, d) *b*-Value determination of the peak cathodic (c) and anodic (d) deformation rate for WO<sub>3</sub> ( $\blacksquare$ ) and WO<sub>3</sub>·2H<sub>2</sub>O ( $\blacktriangle$ ); markers indicate the cathodic and anodic deformation rate peak values at specific sweep rates, and the dashed lines indicate the best linear fit.

rate; that is, the intercalation rate was closely tied to the deformation rate at a particular potential. The deformation rate of the glassy carbon substrate as a function of potential is shown in Figure S4 along with the response of the redox-active tungsten oxides. As expected, glassy carbon exhibits no significant deformation rate since this nonporous electrode exhibits no change in volume during the formation of the electric double layer at its surface.

The observation that the local deformation rate is related to the current is consistent with the report of Tavassol et al., 19 who found that in macroscopic mechanical measurements of the deformation of a graphite electrode during lithiation the derivative of the strain of the entire electrode with respect to the voltage (d $\varepsilon$  d $E^{-1}$ ) scaled with the current (a proof of the consistency between these two observations is included in the Supporting Information). The deformation rate of WO<sub>3</sub>·2H<sub>2</sub>O was smaller and more consistent as a function of potential than for WO<sub>3</sub>, mirroring its nearly symmetric, broad current response in the cyclic voltammogram. In the case of WO<sub>3</sub>, the deformation rate was greater and also asymmetric, similar to its current response. These "deformation rate voltammograms" are shown at 200 mV s<sup>-1</sup>, where the WO<sub>3</sub>·2H<sub>2</sub>O stores more electrons per formula unit than WO<sub>3</sub>. A noteworthy feature of the deformation rate response is that it is only sensitive to energy storage processes that induce a local mechanical response from the electrode material. For instance, no deformation occurs at the cathodic turnover potential, during which the hydrogen evolution reaction occurs at the surface of the electrode (regions indicated by the shaded areas in Figure 3). In other words, the operando AFM dilatometry technique presented here measures the local, nanoscale deformation

response directly induced by electrochemical intercalation with high temporal and spatial resolution.

The clear relationship between deformation and current led us to determine how the deformation rate varied as a function of sweep rate. In electrochemical systems, current that is directly proportional to the sweep rate is said to be surface-limited (capacitive), whereas current that is limited by semi-infinite diffusion will exhibit a square root dependence on the sweep rate.<sup>24</sup> This relationship has been generalized and applied to numerous energy storage materials to determine the extent of capacitive *versus* diffusion-controlled storage:

$$i(E) = av^b (3)$$

Here,  $\nu$  is the cyclic voltammetry sweep rate and a and b are constants. The *b*-value (with limits of  $0.5 \le b \le 1$ ) describes the dependence of the current on the sweep rate, where the limiting values are determined by the rate-limiting mechanisms described above. In a manner similar to eq 3, Figure 4 shows a logarithmic plot of the peak deformation rate as a function of sweep rate; in this type of plot, the slope gives the b-value. In the case of WO<sub>3</sub>·2H<sub>2</sub>O, the peak deformation rate varies with a b-value of ~1 during both proton intercalation and deintercalation. For WO<sub>3</sub>, the peak deformation rate varies with a lower value of ~0.7 during both proton intercalation and deintercalation. This relationship is very similar to what is obtained for the peak current dependence as a function of sweep rate in both WO<sub>3</sub>·2H<sub>2</sub>O and WO<sub>3</sub>,<sup>6</sup> again indicating the strong relationship between the mechanical deformation of the material and the proton intercalation process.

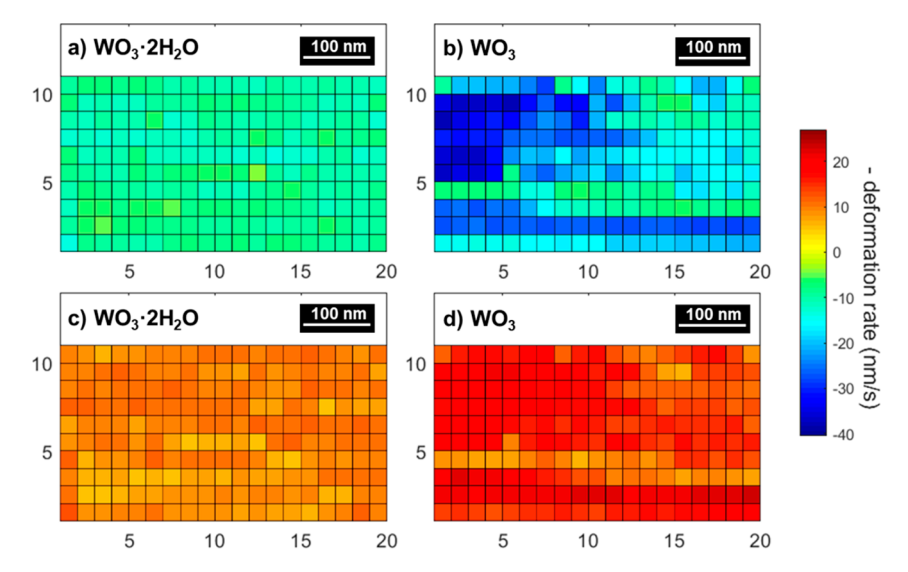


Figure 5. Spatial variation of the local deformation rate of  $WO_3$  and  $WO_3$ : $^2H_2O$  electrodes at the cathodic and anodic peak current potentials. (a, b) Local deformation rate at the cathodic peak current potential for  $WO_3$ : $^2H_2O$  (a) and  $WO_3$  (b). (c, d) Local deformation rate at the anodic peak current potential for  $WO_3$ : $^2H_2O$  (c) and  $WO_3$  (d).

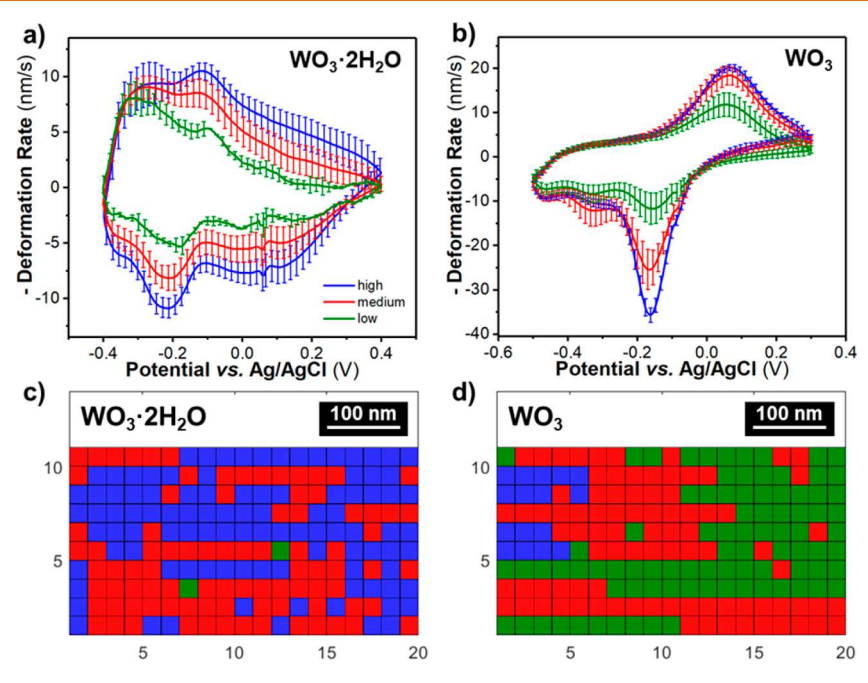


Figure 6. Representative response of regions with low, medium, and high deformation rates. (a, b) Deformation rate versus potential of WO<sub>3</sub>: 2H<sub>2</sub>O (a) and WO<sub>3</sub> (b) extracted from regions with low, medium, and high deformation rates. Error bars indicate the standard deviations of the deformation rate at specific potentials. (c, d) Maps of the locations of regions with low, medium, and high deformation rates in WO<sub>3</sub>: 2H<sub>2</sub>O (c) and WO<sub>3</sub> (d).

To determine whether the results obtained at a single spot on the electrode are representative of the local features of the material, we mapped a 20  $\times$  20 grid of points with 25 nm spacing between each point on the electrodes (an 11  $\times$  20 grid of points was used for quantitative analysis; details in Methods and Experimental). At each point, the local deformation of the electrode was measured as a cyclic voltammetry sweep rate of 200 mV s<sup>-1</sup> was applied to the entire electrode for seven cycles. This experiment allowed for a correlation between the global current measurement and the local, nanoscale electrode deformation. Videos tracking the deformation rate and current as a function of potential at each point for WO<sub>3</sub> and WO<sub>3</sub>· 2H<sub>2</sub>O are available in the Supporting Information. The videos

show that for both materials the deformation rate as a function of potential at each point is qualitatively similar, and therefore the results obtained at a single point are representative of the overall material response. Figure S5 shows the current and average deformation rate as a function of potential. Compared to the graphs obtained from a single point, the averaged graph shows better agreement between the deformation rate peak potentials and the current peak potentials and enhanced signal-to-noise ratio. Figure 5 shows "maps" of the deformation rate and current for the cathodic and anodic peak potentials for WO<sub>3</sub> and WO<sub>3</sub>·2H<sub>2</sub>O (peak potentials are indicated in Figure S6). The deformation rate maps show that while single-point measurement results are qualitatively similar to each other, both

electrodes exhibit spatial inhomogeneity. The inhomogeneity is visualized in Figure 6, which shows the average deformation rate *versus* potential collected from regions with low, medium, and high deformation rates. The inhomogeneity can be attributed to the variation of the electrode thickness and particle orientation observed in the SEM micrographs in Figure S1.

Overall, this technique presents a method to correlate global electrochemical measurements with local deformation in energy storage materials. The advantages of this technique include an indirect measurement of local electrochemical activity with an axial resolution of up to 0.1 nm, a lateral resolution of tens of nanometers, and a temporal resolution as high as 100  $\mu$ s. There are several limitations to this method. The first limitation comes from the AFM instrument. The scan size is usually limited to below 150  $\times$  150  $\mu$ m. The second limit may come from the time it takes to scan and perform dilatometry over a large area, as in the meantime the sample may undergo degradation or drift of position, or the electrochemical cell may change (due to electrolyte evaporation, reference electrode drift, etc.). Due to the nature of AFM probes, sample areas that contain steep walls and overhangs should be avoided. While the ideal sample for AFM would be an epitaxial thin film with wellcontrolled crystallographic orientation and thickness, our results show the versatility of the technique in that good results are possible even with more disordered drop-cast and porous electrodes.

To understand the differences in the deformation of WO<sub>3</sub>. nH<sub>2</sub>O electrodes during proton intercalation, we investigated the materials' structural evolution using ex situ X-ray diffraction (XRD). WO<sub>3</sub> (Figure S7) undergoes a reversible phase transition, whose onset and disappearance coincides with the cathodic and anodic redox peaks, respectively, of the cyclic voltammogram. Prior reports of H<sup>+</sup> and Li<sup>+</sup> intercalation into monoclinic WO<sub>3</sub> have determined that at the level of intercalation investigated here  $(H_{0.12}WO_3)$ , there is an electrochemically reversible phase transition to the tetragonal structure,  $^{25-27}$  and at  $H_{0.23}WO_3$ , this transition leads to a volume expansion of 1.77% from the pristine monoclinic WO<sub>3</sub>.<sup>28</sup> While this expansion is of the same sign and order of magnitude as the results obtained with operando AFM dilatometry, the unit cell volume expansion obtained from refinement of XRD patterns is smaller. The difference is attributed to the complexity of our drop-cast thin film electrodes, where orientation of the particles and porosity could contribute to the deformation magnitude. As shown in Figure S8a, the results presented here agree with these prior reports in that at a potential of  $-0.2 \text{ V} (H_{0.12}\text{WO}_3)$  the structure can be indexed to that of tetragonal H<sub>0.1</sub>WO<sub>3</sub>.<sup>27</sup> The variation in XRD peak widths in Figure S8a is not consistent, which is attributed to the presence of two related monoclinic phases in the pristine WO<sub>3</sub> (Figure S8b).<sup>6,29</sup> WO<sub>3</sub>·2H<sub>2</sub>O also undergoes a reversible phase transition whose existence is bound by the cathodic and anodic redox peaks (Figure S9). Importantly, these results show that for intercalation levels of up to  $H_{0.1}WO_3 \cdot 2H_2O$  (-0.2 V) there is no visible change of the (010) interlayer spacing. This has been attributed to the absence of proton storage sites in the hydrated interlayer of WO<sub>3</sub>·2H<sub>2</sub>O.<sup>30</sup> The primary structural differences before and after the phase transition are the merging of diffraction peaks between ~22.5° and 27.5°. Laurinavichute et al.<sup>31</sup> also observed the merging of these peaks with chemical intercalation of protons into WO<sub>3</sub>·2H<sub>2</sub>O. Prior reports indicate that the phase

transition is likely due to a structural transformation toward a more symmetric crystal structure via increasing orthogonality of  $WO_5(OH_2)$  octahedra $^{31-33}$  due to the storage of protons in the octahedral tungsten oxide layer. The distortion of  $WO_3$ ·  $2H_2O$  due to proton intercalation is therefore only two-dimensional, whereas the distortion of  $WO_3$  is three-dimensional. This difference in structural distortion between the  $WO_3$  structure and  $WO_3$ · $2H_2O$  may contribute to the more irreversible electrochemical intercalation kinetics in the former, resulting in the previously reported transition from battery to pseudocapacitive behavior via structural water.

The results presented here demonstrate that  $WO_3 \cdot 2H_2O$  and  $WO_3$  exhibit different deformation behavior during the storage of protons. As indicated by the *ex situ* XRD results shown here and reported previously, both  $WO_3 \cdot 2H_2O$  and  $WO_3$  undergo phase transitions upon intercalation of  $H^+$ . However, in the material with structural water, the mechanism is kinetically surface-limited and highly reversible, whereas in the anhydrous material, it is diffusion-limited and more irreversible. The differences in the mechanical response and kinetics between these two materials may be due to the difference in the number of primary bonds that undergo distortion during proton intercalation and deintercalation and the role of interlayer structural water in confining distortion into only two dimensions.

WO<sub>3</sub> exhibits a distorted ReO<sub>3</sub>-type structure, where each WO<sub>6</sub> octahedron is corner sharing in three dimensions. WO<sub>3</sub>. 2H<sub>2</sub>O is made up of WO<sub>5</sub>(OH<sub>2</sub>) octahedra that are also corner sharing, but only in two dimensions; the corner-sharing octahedra layers are separated from each other by structural water molecules (Figure S10). In both materials, the proton intercalation site has been hypothesized as the octahedral site between the bridging oxygens of tungsten octahedra. 33,34 The primary structural differences in this site in WO<sub>3</sub>·2H<sub>2</sub>O are that there is an interlayer water molecule above and below the site and that  $WO_5(OH_2)$  octahedra are not connected to each other via primary bonds between layers. The separation of these twodimensional layers by structural water may lead to much more facile and flexible mechanical deformation during proton intercalation than in WO3, where the WO6 octahedra effectively undergo three-dimensional distortion during ion intercalation. The apparent lack of proton intercalation sites within the structural water layer in WO<sub>3</sub>·2H<sub>2</sub>O is also quite different from the intercalation behavior of other layered oxides with structural water and may explain why the kinetic behavior of this material is particularly fast.

# **CONCLUSIONS**

Our results imply that for a material to possess high rate capability it not only needs high electronic and ionic conductivity but also a flexible structure to accommodate the structural distortion due to ion storage. These results also demonstrate a powerful and versatile *operando* AFM technique for measuring local electro-chemo-mechanical coupling in materials, opening the door for improved understanding of mechanisms of energy storage in materials as well their degradation processes. In the future, this technique can be expanded to map out the details of local redox processes or applied to single-particle electrodes that cannot be measured with standard electrochemical techniques.

#### **METHODS AND EXPERIMENTAL**

**Synthesis.**  $WO_3 \cdot 2H_2O$  was synthesized through a room-temperature acid precipitation method as described by Freedman. <sup>35</sup>  $WO_3$  was obtained through thermal dehydration of  $WO_3 \cdot 2H_2O$  at 350 °C in air.

Thin Film Electrode Preparation for *Operando* AFM Measurements. WO<sub>3</sub>·nH<sub>2</sub>O thin films for the *operando* AFM dilatometry measurements were drop cast from *N*-methyl-2-pyrrolidone (NMP, Sigma-Aldrich) onto circular glassy carbon substrates (HTW-Germany). The solutions consisted of 95% w/w active material (WO<sub>3</sub>·nH<sub>2</sub>O) and 5% w/w polyvinylidene fluoride binder (PVDF, Arkema). Substrates were air-dried overnight before a final oven drying step for 30 min. Anhydrous WO<sub>3</sub> films were dried at 130 °C, and WO<sub>3</sub>·2H<sub>2</sub>O films were dried at 75 °C to prevent dehydration. Resulting films had a total mass loading of 100 µg cm<sup>-2</sup>.

Electrode Preparation for Ex Situ X-ray Diffraction. The anhydrous WO<sub>3</sub> slurry was made as described previously. WO<sub>3</sub>·2H<sub>2</sub>O electrodes were fabricated by mixing an aqueous solution of WO<sub>3</sub>·2H<sub>2</sub>O (16% w/v) with a slurry consisting of acetylene black (4% w/v) (Alfa Aesar) and PVDF (4% w/v) in NMP. The resulting mixture had a composition of 80% w/w WO<sub>3</sub>·2H<sub>2</sub>O, 10% w/w acetylene black, and 10% w/w PVDF. Electrodes for the ex situ studies were made by painting the slurry onto platinized silicon wafers (Radiant Technologies, Inc.) and drying at 50 °C. Mass loadings for ex situ measurements were controlled at 4–5 mg cm<sup>-2</sup>.

Characterization. Operando Atomic Force Microscopy Dilatometry. Operando AFM dilatometry measurements were conducted using a commercial in situ electrochemical AFM cell (Figure S2) and MFP-3D atomic force microscope (both from Asylum Research, USA) with Pt-coated AFM tips (Nanosensors, PPP-EFM-50, k = 0.5-9.5 N m<sup>-1</sup>). Electrode deformation measurements were obtained using two methods. For deformation measurement on individual spots, a constant force mode was used. For the 20 × 20 point grid mapping with a spacing of 25 nm, the AFM cantilever performed a forcedistance curve at each spot and triggered the potentiostat to run cyclic voltammetry at 200 mV s<sup>-1</sup> for seven cycles during the contact part of the force-distance curve. After the cyclic voltammetry was finished, the cantilever withdrew and moved to the next spot. The above procedure was repeated for all 400 points on the grid. The deformation was recorded by the deflection of the cantilever. Electrochemical characterization was performed with a Bio-Logic SP-300 potentiostat (Bio-Logic, USA) in a three-electrode configuration with Ag/AgCl reference and activated carbon counter electrodes in 0.5 M H<sub>2</sub>SO<sub>4</sub> as the electrolyte. The EC-Lab software (Bio-Logic) recorded the time, potential of the working electrode, current, and deformation signal from the microscope in units of volts. The conversion of the deformation signal to the unit of length was obtained by taking the slope of the retraction part of the force-distance curve.

Ex Situ X-ray Diffraction. X-ray diffraction was performed on a PANalytical Empyrean X-ray diffractometer in standard Bragg-Brentano geometry with Cu K\alpha radiation. Ex situ measurements for anhydrous WO3 were performed in a nitrogen atmosphere with the Anton Paar TTK 450 chamber. Measurements for WO3·2H2O were conducted in an ambient atmosphere to prevent dehydration. Diffraction patterns were collected for both phases at various potentials as noted in the main text in order to determine the structural evolution as a function of potential. Electrochemical measurements were conducted in a three-electrode beaker cell with Ag/AgCl reference and platinum wire counter electrodes in a 0.5 M H<sub>2</sub>SO<sub>4</sub> electrolyte. The potential of the working electrode was controlled with a WaveNow<sup>XV</sup> potentiostat (Pine Instruments) using linear sweep voltammetry (LSV) at a sweep rate of 5 mV s<sup>-1</sup>. After the LSV scan finished, the electrode was immediately removed from solution, rinsed with deionized water, dried with compressed air, and placed into the diffractometer. The same electrode was used throughout the ex situ experiment. After one XRD measurement and before the next LSV scan, the electrode was held at either the opencircuit potential (cathodic scans) or -0.2 V (anodic scans).

**Data Analysis.** Analysis of Operando AFM Deformation Data. To obtain the electrode deformation rate, a set of data-smoothing procedures was applied to the original deformation data,  $\delta(E)$ . The

high-frequency noise was smoothed by a Savitzky-Golay filter, and then a background subtraction was applied to remove the lowfrequency background variation. The derivative of the smoothed deformation data was taken with respect to time to obtain the deformation rate,  $d\delta(E)$  dt<sup>-1</sup>. Due to the sensitivity of the derivative, the deformation rate data were smoothed with a second Savitzky-Golay filter. The negative deformation rate was used in the graphs to aid visual observation and in the main text was referred to as "deformation rate". A negative deformation rate indicates expansion of the electrode, while a positive deformation rate indicates contraction. For the mapping data, note that, due to external interferences including reference potential drift during measurement for WO<sub>3</sub>·2H<sub>2</sub>O and software glitches for  $WO_3$ , only the first  $11 \times 20$  grid of points was used for quantitative analysis. Full maps with a  $20 \times 20$  grid of points at the anodic and cathodic peak current potentials are presented in Figure S11. The criteria for selecting regions with low, medium, and high deformation rates in WO<sub>3</sub> and WO<sub>3</sub>·2H<sub>2</sub>O are displayed in Table

Table 1. Ranges of Low, Medium, and High Deformation Rates in WO<sub>3</sub> and WO<sub>3</sub>·2H<sub>2</sub>O Used for Figure 6<sup>a</sup>

electrode	range of low deformation rate $(nm s^{-1})$	range of medium deformation rate $(nm s^{-1})$	range of high deformation rate $(nm s^{-1})$
$WO_3$	−0.13 to −0.02	−0.24 to −0.13	−0.35 to −0.24
$WO_3$ ·	-0.04 to $-0.01$	-0.07 to $-0.04$	-0.14 to $-0.07$
$2H_2O$			

<sup>a</sup>To generate these ranges, the deformation rates at each spot at the cathodic peak potential were grouped together and analyzed with a histogram.

## ASSOCIATED CONTENT

# S Supporting Information

The Supporting Information is available free of charge on the ACS Publications website at DOI: 10.1021/acsnano.8b02273.

Derivation of our results' consistency with ref 19, SEM micrographs, schematic of the AFM cell, specific capacitance of the electrodes, comparison of deformation rate of electrodes to the background, average deformation rates of the electrodes, cyclic voltammograms,  $ex\ situ\ XRD$  patterns, crystallographic structures, and  $20\times 20\ maps\ (PDF)$ 

Movie of WO<sub>3</sub> local displacement rate and global current as a function of potential, (AVI)

Movie of WO<sub>3</sub>·2H<sub>2</sub>O local displacement rate and global current as a function of potential (AVI)

## **AUTHOR INFORMATION**

#### **Corresponding Author**

\*E-mail: vaugust@ncsu.edu.

ORCID

Nina Balke: 0000-0001-5865-5892

Veronica Augustyn: 0000-0001-9885-2882

Notes

The authors declare no competing financial interest.

## **ACKNOWLEDGMENTS**

We thank A. Costine with initial assistance on *operando* AFM measurements and C.-C. Chung for assistance with *ex situ* XRD measurements. This material is based upon work supported by the National Science Foundation under Grant No. 1653827 and by the National Science Foundation Graduate Research

Fellowship Program under Grant No. 571800 (to S.B.). W.-Y.T. and Q.G. were supported as part of the Fluid Interface Reactions, Structures and Transport (FIRST) Center, an Energy Frontier Research Center funded by the U.S. Department of Energy, Office of Science, Office of Basic Energy Sciences. *Operando* AFM was conducted at the Center for Nanophase Materials Sciences, which is a DOE Office of Science User Facility. V.A. also acknowledges support from the Ralph E. Powe Junior Faculty Enhancement Award.

## **REFERENCES**

- (1) Whittingham, M. Insertion Electrodes as Smart Materials: The First 25 Years and Future Promises. *Solid State Ionics* **2000**, *134*, 169–178.
- (2) Braun, P. V.; Cho, J.; Pikul, J. H.; King, W. P.; Zhang, H. High Power Rechargeable Batteries. *Curr. Opin. Solid State Mater. Sci.* **2012**, *16*, 186–198.
- (3) Augustyn, V.; Simon, P.; Dunn, B. Pseudocapacitive Oxide Materials for High-Rate Electrochemical Energy Storage. *Energy Environ. Sci.* **2014**, *7*, 1597–1614.
- (4) Gogotsi, Y.; Penner, R. M. Energy Storage in Nanomaterials Capacitive, Pseudocapacitive, or Battery-Like? *ACS Nano* **2018**, *12*, 2081–2083.
- (5) Palacín, M. R.; Simon, P.; Tarascon, J. M. Nanomaterials for Electrochemical Energy Storage: the Good and the Bad. *Acta Chim. Slov.* **2016**, *63*, 417–423.
- (6) Mitchell, J. B.; Lo, W. C.; Genc, A.; LeBeau, J.; Augustyn, V. Transition from Battery to Pseudocapacitor Behavior *via* Structural Water in Tungsten Oxide. *Chem. Mater.* **2017**, *29*, 3928–3937.
- (7) Reichman, B.; Bard, A. J. The Electrochromic Process at WO<sub>3</sub> Electrodes Prepared by Vacuum Evaporation and Anodic Oxidation of W. J. Electrochem. Soc. **1979**, 126, 583–591.
- (8) Judeinstein, P.; Livage, J. Role of the Water Content on the Electrochromic Properties of WO<sub>3</sub>, nH<sub>2</sub>O Thin Films. *Mater. Sci. Eng., B* **1989**, 3, 129–132.
- (9) Kattouf, B.; Frey, G. L.; Siegmann, A.; Ein-Eli, Y. Enhanced Reversible Electrochromism *via In Situ* Phase Transformation in Tungstate Monohydrate. *Chem. Commun.* **2009**, *0*, 7396–7398.
- (10) Nam, K. W.; Kim, S.; Lee, S.; Salama, M.; Shterenberg, I.; Gofer, Y.; Kim, J.-S.; Yang, E.; Park, C. S.; Kim, J.-S.; Lee, S.-S.; Chang, W.-S.; Doo, S.-G.; Jo, Y. N.; Jung, Y.; Aurbach, D.; Choi, J. W. The High Performance of Crystal Water Containing Manganese Birnessite Cathodes for Magnesium Batteries. *Nano Lett.* **2015**, *15*, 4071–4079.
- (11) Kundu, D.; Adams, B. D.; Duffort, V.; Vajargah, S. H.; Nazar, L. F. A High-Capacity and Long-Life Aqueous Rechargeable Zinc Battery Using a Metal Oxide Intercalation Cathode. *Nat. Energy* **2016**, *1*, 16119.
- (12) Novák, P.; Scheifele, W.; Joho, F.; Haas, O. Electrochemical Insertion of Magnesium into Hydrated Vanadium Bronzes. *J. Electrochem. Soc.* **1995**, 142, 2544–2550.
- (13) Augustyn, V.; Gogotsi, Y. 2D Materials with Nanoconfined Fluids for Electrochemical Energy Storage. *Joule* **2017**, *1*, 443–452.
- (14) Huang, J. Y.; Zhong, L.; Wang, C. M.; Sullivan, J. P.; Xu, W.; Zhang, L. Q.; Mao, S. X.; Hudak, N. S.; Liu, X. H.; Subramanian, A.; Fan, H.; Qi, L.; Kushima, A.; Li, J. *In Situ* Observation of the Electrochemical Lithiation of a Single SnO<sub>2</sub> Nanowire Electrode. *Science* **2010**, 330, 1515–1520.
- (15) Levi, E.; Levi, M. D.; Chasid, O.; Aurbach, D. A Review on the Problems of the Solid State Ions Diffusion in Cathodes for Rechargeable Mg Batteries. *J. Electroceram.* **2009**, 22, 13–19.
- (16) Pharr, M.; Zhao, K.; Wang, X.; Suo, Z.; Vlassak, J. J. Kinetics of Initial Lithiation of Crystalline Silicon Electrodes of Lithium-Ion Batteries. *Nano Lett.* **2012**, *12*, 5039–5047.
- (17) Black, J. M.; Feng, G.; Fulvio, P. F.; Hillesheim, P. C.; Dai, S.; Gogotsi, Y.; Cummings, P. T.; Kalinin, S. V.; Balke, N. Strain-Based *In Situ* Study of Anion and Cation Insertion into Porous Carbon Electrodes with Different Pore Sizes. *Adv. Energy Mater.* **2014**, *4*, 1300683.

- (18) Come, J.; Black, J. M.; Lukatskaya, M. R.; Naguib, M.; Beidaghi, M.; Rondinone, A. J.; Kalinin, S. V.; Wesolowski, D. J.; Gogotsi, Y.; Balke, N. Controlling the Actuation Properties of MXene Paper Electrodes upon Cation Intercalation. *Nano Energy* **2015**, *17*, 27–35.
- (19) Tavassol, H.; Jones, E. M. C.; Sottos, N. R.; Gewirth, A. A. Electrochemical Stiffness in Lithium-Ion Batteries. *Nat. Mater.* **2016**, *15*, 1182–1188.
- (20) Hantel, M.; Presserb, V.; Kötza, R.; Gogotsi, Y. *In Situ* Electrochemical Dilatometry of Carbide-Derived Carbons. *Electrochem. Commun.* **2011**, *13*, 1221–1224.
- (21) Jäckel, N.; Dargel, V.; Shpigel, N.; Sigalov, S.; Mikhael, L.; Daikhin, L.; Aurbach, D.; Presser, V. *In Situ* Multi-Length Scale Approach to Understand the Mechanics of Soft and Rigid Binder in Composite Lithium Ion Battery Electrodes. *J. Power Sources* **2017**, *371*, 162–166.
- (22) Schiffer, Z. J.; Cannarella, J.; Arnold, C. B. Strain Derivatives for Practical Charge Rate Characterization of Lithium Ion Electrodes. *J. Electrochem. Soc.* **2016**, *163*, A427—A433.
- (23) Granqvist, C. G. Handbook of Inorganic Electrochromic Materials; Elsevier, 1995.
- (24) Bard, A. J.; Faulkner, L. R. Electrochemical Methods: Fundamentals and Applications; John Wiley & Sons, Inc.: New York, 2001.
- (25) Strømme Mattsson, M. Cation Intercalation in Sputter-Deposited W Oxide Films. *Phys. Rev. B: Condens. Matter Mater. Phys.* **1998**, *58*, 11015–11022.
- (26) Zhong, Q.; Dahn, J. R.; Colbow, K. Lithium Intercalation into WO<sub>3</sub> and the Phase Diagram of Li<sub>x</sub>WO<sub>3</sub>. *Phys. Rev. B: Condens. Matter Mater. Phys.* **1992**, *46*, 2554–2560.
- (27) Ampe, B.; Leroy, J. M.; Thomas, D.; Tridot, G. Contribution to the Study of Systems: Tungsten-Oxygen and Tungsten-Vanadium-Oxygen. *Rev. Chim. Miner.* **1968**, *5*, 801.
- (28) Guéry, C.; Choquet, C.; Dujeancourt, F.; Tarascon, J. M.; Lassègues, J. C. Infrared and X-Ray Studies of Hydrogen Intercalation in Different Tungsten Trioxides and Tungsten Trioxide Hydrates. *J. Solid State Electrochem.* **1997**, *1*, 199–207.
- (29) Righettoni, M.; Tricoli, A.; Pratsinis, S. E. Thermally Stable, Silica-Doped  $\varepsilon$ -WO $_3$  for Sensing of Acetone in the Human Breath. *Chem. Mater.* **2010**, 22, 3152–3157.
- (30) Lin, H.; Zhou, F.; Liu, C.-P.; Ozolins, V. Non-Grotthuss Proton Diffusion Mechanism in Tungsten Oxide Dihydrate from First-Principles Calculations. *J. Mater. Chem. A* **2014**, *2*, 12280–12288.
- (31) Laurinavichute, V. K.; Vassiliev, S. Y.; Khokhlov, A. A.; Plyasova, L. M.; Molina, I. Y.; Tsirlina, G. A. Electrodeposited Oxotungstate Films: Towards the Molecular Nature of Recharging Processes. *Electrochim. Acta* **2011**, *56*, 3530–3536.
- (32) Pugolovkin, L. V.; Cherstiouk, O. V.; Plyasova, L. M.; Molina, I. Y.; Kardash, T. Y.; Stonkus, O. A.; Yatsenko, D. A.; Kaichev, V. V.; Tsirlina, G. A. Electrodeposited Non-Stoichiometric Tungstic Acid for Electrochromic Applications: Film Growth Modes, Crystal Structure, Redox Behavior and Stability. *Appl. Surf. Sci.* **2016**, *388*, 786–793.
- (33) Dickens, P. G.; Kay, S. A.; Crouch-Baker, S.; Claridge, D. A. Thermochemistry of the Hydrogen Insertion Compounds Formed by the Molybdic and Tungstic Acids  $H_xMO_3 \cdot nH_2O$  (M=Mo, n=1; M=W, n=1,2). Solid State Ionics 1987, 23, 9–14.
- (34) Granqvist, C. G. Electrochromic Tungsten Oxide Films: Review of Progress 1993–1998. *Sol. Energy Mater. Sol. Cells* **2000**, *60*, 201–262.
- (35) Freedman, M. L. The Tungstic Acids. J. Am. Chem. Soc. 1959, 81, 3834–3839.